Table of contents

By introducing different boron-containing guests into ZIF-8 hosts *via* an integrated double-solvent impregnation and refined-etching method, ZIF-8 derived B,N@C-AB and B,N@C-BA hierarchical porous carbon frameworks were synthesized. The B,N@Cs displayed high catalytic activities for electrochemical oxygen reduction reaction, and the enhancement is due to the coexistence of B and N and the mass transfer promoted by the unique hierarchical porous structure.

Xuefei Wang, Chao Han, Haitao Li, Panpan Su, Na Ta, Yanfu Ma, Zhenguo Huang, and Jian Liu,**

Fabrication of highly B, N co-doped hierarchical porous carbon through confined etching to boost electrocatalytic oxygen reduction

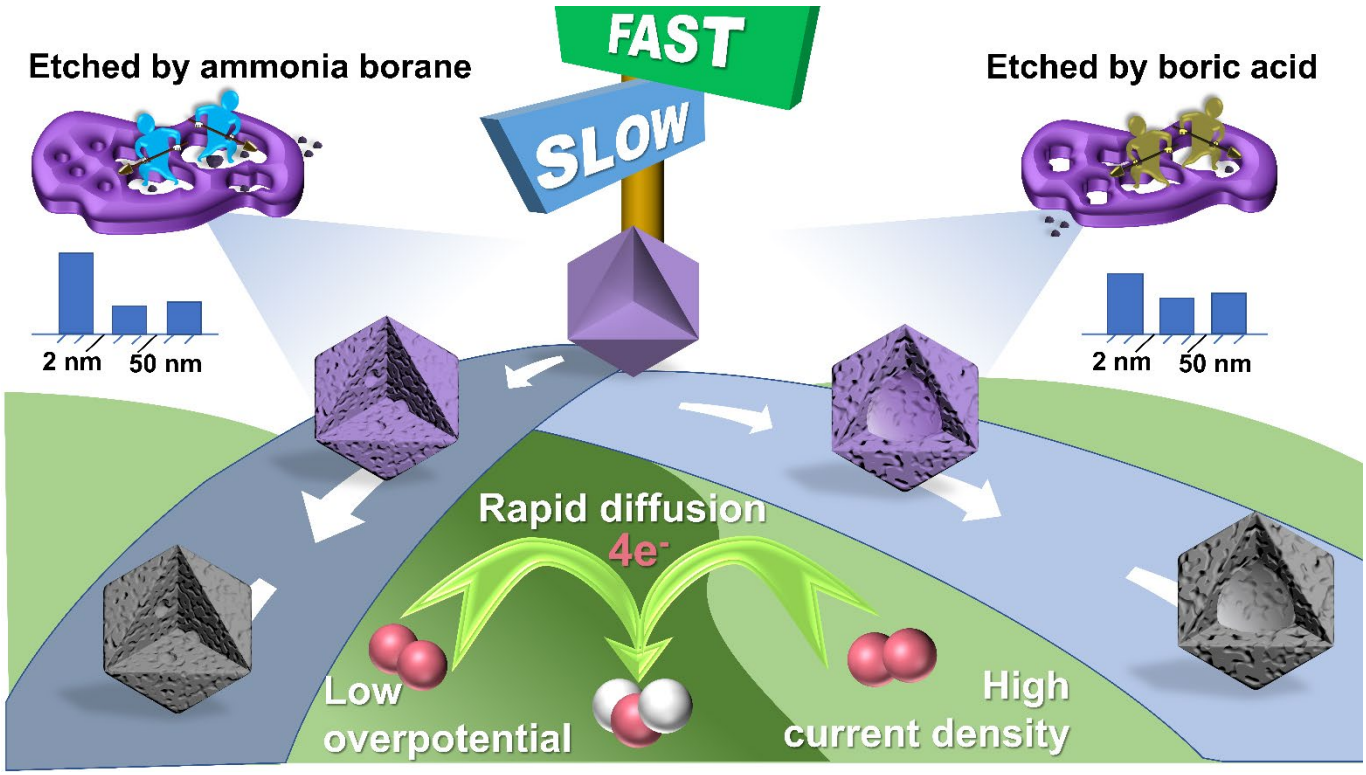

Fabrication of highly B, N co-doped hierarchical porous carbon through confined etching to boost electrocatalytic oxygen reduction

Xuefei Wang,[1,2] Chao Han,[1] Haitao Li,[2] Panpan Su,[2] Na Ta,[2] Yanfu Ma,[2] Julie M. Cairney[3], Zhenguo Huang,[1] and Jian Liu,*[2,4]*

[1] School of Civil & Environmental Engineering, University of Technology Sydney, Sydney, NSW, 2007, Australia

[2] State Key Laboratory of Catalysis, Dalian Institute of Chemical Physics, Chinese Academy of Sciences, 457 Zhongshan Road, Dalian 116023, China

[3] Australian Centre for Microscopy and Microanalysis, the University of Sydney, Sydney, NSW, 2006 Australia

[4] DICP-Surrey Joint Centre for Future Materials, University of Surrey Guildford, Surrey, GU2 7XH, UK

Address correspondence to Zhenguo Huang, zhenguo.huang@uts.edu.au; Jian Liu, jian.liu@surrey.ac.uk

Abstract

Dual heteroatom-doped carbons have attracted widespread research attention as catalysts in the field of energy storage and conversion due to their unique electronic structures and chemical tunability. In particular, boron and nitrogen co-doped carbon (B,N@C) has been shown great potential for photo/electrocatalytic applications. However, more needs to be done to rationally design and regulate the structure of these materials to improve their catalytic performance. Herein, hierarchical porous B,N@C was fabricated by pyrolyzing Zeolite imidazole framework (ZIF) which was treated with ammonia borane or boric acid via an integrated double-solvent impregnation and confined-etching method. The treated ZIF-8 provides an essential structural template to achieve B, N co-doped hierarchical structures with micro/meso/macro multimodal pore size distributions. The resultant B,N@C frameworks displayed high catalytic activities for electrochemical oxygen reduction reaction (ORR) in alkaline media, outperforming most carbon-based catalysts, particularly from the perspective of the half-wave potentials. Such high catalytic performance is due to the enhanced activity by the coexistence of B and N and the mass transfer promoted by the unique hierarchical porous structure.

Keywords

Heteroatom doping; Hierarchical porous carbon; Host–guest chemistry; Confined etching; Electrocatalysis; Mass transfer

1. Introduction

Metal-organic frameworks (MOFs), which consist of metal nodes and organic ligands, are desirable precursors and templates for metal/carbon-based nanostructures used in diverse applications including energy storage and conversion [1-3]. Zeolite imidazole frameworks (ZIFs) are a subclass of MOFs, featuring high N content, large surface areas, and ordered porous textures [4]. Because of these special

features, ZIFs can act as ideal sacrificial templates and precursors to generate porous nitrogen-doped carbons (N@Cs) used in electrochemical energy storage and conversion [5-7]. However, the direct pyrolysis of ZIFs under a high temperature often leads to micropore-dominated structures with poor conductivity, which limits their performance [8-10]. The structures and functions of ZIFs-derived N@Cs could be tuned by controlling the precursor composition via introducing templates, pore-forming agents, and dopants [11, 12].

Dual, ternary, and quaternary heteroatom-doping (N/B, N/P, N/S, N/O, N/B/P, N/S/P, N/B/S/P, etc.) can dramatically improve the performance of carbon in many applications [13-17]. Among these heteroatoms, N and B are of particular interest as co-dopant, since they are next to carbon (C) in the periodic table, and are of similar atomic sizes. The electronegativity of B (2.04) and N (3.04) is lower and higher than that of C (2.55), respectively. B can further substitute C in N@C lattice and lead to the synergistic effect induced by the pairing and/or long-range coupling, which alters the electronic and charges density and consequently chemical properties [18-21]. B, N co-doped carbons (B,N@Cs), as metal-free ternary materials, have shown great potential for energy storage and conversion devices [18, 21-32].

There have been reports on synthesizing MOF-derived B-containing carbon nanostructures by directly pyrolyzing B-containing MOF (e.g. BIF-82 [33] and BIF-1S [34]) and the mixture of MOFs with B-containing substances [17, 35-43]. However, most of these B-containing carbon nanomaterials displayed collapsed structure of MOFs, because to get the reasonably homogeneous distribution of B elements, aqueous solutions were employed to mix MOFs with B-containing precursors, and MOFs are sensitive to water. As such, B-containing carbon nanomaterials obtained after pyrolysis exhibited irregular morphologies [37-43]. Furthermore, most of these resulted B-containing carbon nanomaterials possessed predominantly microporous structures [17, 36-41]. The efficiency of mass transport and reactant diffusion is quite restricted by the micropores. Typically, micropores (<2 nm) lead to high surface area, and large numbers of active sites; mesopores (2-50 nm) contribute to local accessibility through a shortened diffusion length; macropores (>50 nm) provide an interconnected and stable framework with superior

mass long-range transfer [12, 44]. Therefore, it is desired to have structures with micro-, meso-, and macropores. Moreover, the doping amounts of B in the reported ZIF-8 derived B,N@C are rather low (usually <6 at%) [17, 33-37, 39, 40, 42].

Herein, we employed a host-guest chemical strategy to immobilize boron species into the cavities of a ZIF and achieved a high doping content of B (15 at%). It is known that small organic and inorganic compounds (e.g. CH_4 [45], N_2 [45], $FeCl_3$ [46], $PdCl_2$ [47], $CuCl_2$ [47], and thiourea [48, 49] can be absorbed or introduced into ZIF-8s through their channels. Occasionally, even a guest molecule (Rhodamine 6G) larger than both aperture and pore sizes of ZIF-8 can be successfully incorporated into ZIF-8 when ligand dissociation occurred during the incorporating process [50]. In our study, during the integrated process of double-solvent impregnation (DSI) and confined-etching (Fig. 1), guest molecules such as ammonia borane (AB) and boric acid (BA) dispersed into the pores of the ZIF-8 act as B source and also as an etching agent to *in-situ* enlarge the pores of ZIF-8 hosts. The trapped AB or BA was then thermally decomposed and anchored in the N@C frameworks, forming B,N@C containing micro-, meso-, and macro multimodal porosities. The combination of the unique hierarchical structure and the synergetic effect between the heteroatoms renders the resulting B,N@C an ideal catalyst for electrochemical oxygen reduction reaction (ORR) in alkaline electrolytes (half-wave potentials as high as 895 mV). This work reveals a novel strategy to achieve hierarchical porous B,N@C catalysts which can be used in various energy conversion and storage applications.

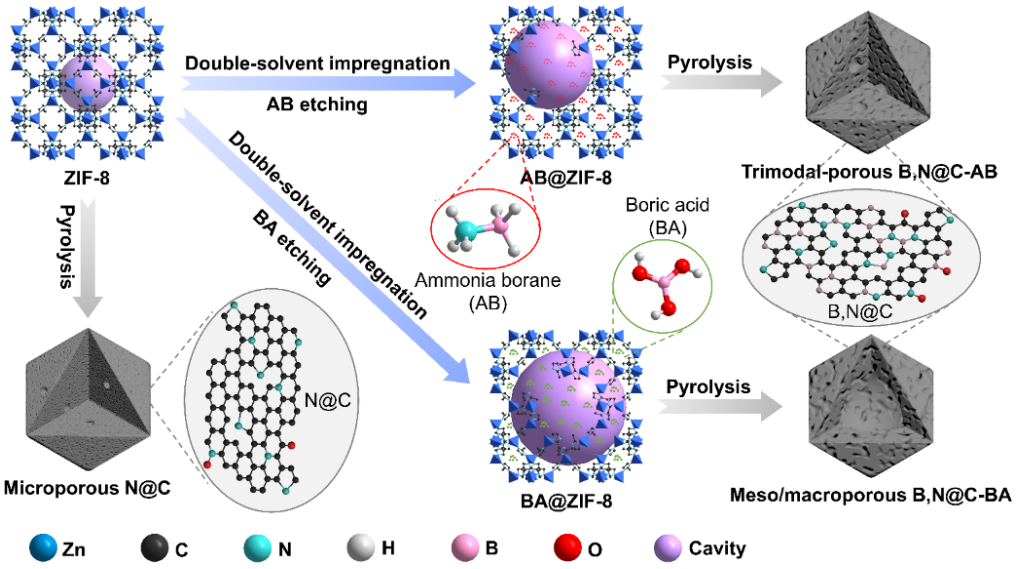

Fig. 1. Schematic diagram of the fabrication of B,N@C nanomaterials.

2. Experiment

2.1 Chemicals

Zinc nitrate hexahydrate ($Zn(NO_3)_2 \cdot 6H_2O$), 2-methylimidazole (2-MIM), boric acid ($B(OH)_3$), cyclohexane, methanol, and ethanol were purchased from Chinese Medicine Group. Ammonia borane (AB) was purchased from Macklin Co., Ltd. Commercial 20 wt% Pt/C was purchased from Alfa Aesar Chemical Reagent Co., Ltd. Nafion (5 wt %) was purchased from Sigma-Aldrich. All chemicals were of analytical grade and used without further purification. Deionized water was used for all experiments.

2.2 Synthesis of ZIF-8

$Zn(NO_3)_2 \cdot 6H_2O$ (0.89 g) and 2-MIM (1.970 g) were first dissolved in methanol, respectively. Then methanol of 2-MIM was added to methanol of $Zn(NO_3)_2 \cdot 6H_2O$. The solution was stirred for 24 hours. The resultant white precipitate was obtained, washed, and dried for further use.

2.3 Synthesis of AB@ZIF-8 and BA@ZIF-8 composites

100 mg of the as-prepared ZIF-8 powders were dispersed in 20 mL of cyclohexane assisted by ultrasonication. Then a 100 μL of ammonia borane aqueous solution (100 mg/mL) was added into ZIF-8 dispersion dropwise. The AB@ZIF-8 composite was collected by centrifugation after impregnation for

3h. Similarly, 100 μL boric acid aqueous solution (51 mg/mL) was used to prepare BA@ZIF-8. To introduce the same amount of B into ZIF-8 host, the impregnation of AB was repeated 4 times.

2.4 Synthesis of N@C, B,N@C-AB, and B,N@C-BA

To obtain N@C and B,N@C, 300 mg of the ZIF-8, BA@ZIF-8, and AB@ZIF-8 were heated at 1000 °C for 2 h with a ramping rate of 2 °C min^{-1} under N_2 atmosphere, respectively.

2.5 Characterization

Transmission electron microscope (TEM) observations were carried out on a Hitachi HT7700 TEM system operated at 100 kV. The aberration-corrected high-angle annular dark-field scanning transmission electron microscopy (HAADF-STEM) measurements were performed on the JOEL's JEM-ARM200F, which was also used to collect energy-dispersive X-ray spectra (EDS). The morphologies were observed by a JSM-7900F field emission scanning electron microscope (SEM) at an accelerating voltage of 2 kV. Wide-angle powder X-ray diffraction (PXRD) patterns were obtained on a Rigaku SmartLab diffractometer with Cu K_α radiation (λ = 1.5418 Å) at a scanning rate of 20°/min. Nitrogen adsorption-desorption data were obtained at -196 °C (Micromeritcs ASAP 2460). X-ray photoelectron spectroscopy (XPS) was conducted on Thermo Scientific K-Alpha apparatus with monochrome Al K_α as the excitation light source. All the binding energies were referenced to C 1s standard peak at 284.8 eV.

2.6 Electrochemical measurements

All the electrochemical measurements were carried out using an electrochemical workstation (PARSTAT 3000A-DX) with a three-electrode system. An Ag/AgCl electrode (saturated KCl), a Pt wire, and a rotating ring-disk electrode (RRDE) coated with catalysts were used as the reference electrode, counter electrode, and working electrode, respectively. The RRDE assembly consists of a glassy carbon rotation disk electrode (disk area: 0.247 cm^2) and a Pt ring (ring area: 0.186 cm^2), with a theoretical collection efficiency (N) of 37%. The working electrode was fabricated by dispersing 5 mg as-prepared materials in 175 μL of ethanol and 47.5 μL of 5 wt% Nafion. 7 μL of the catalyst ink was dropped onto

the disk electrode for the RRDE measurement. The transferred electron numbers (n) and H_2O_2 (H_2O_2%) selectivity were calculated based on the disk current (I_d) and ring current (I_r) from RRDE as the following equation.

$$n=\frac{4I_d}{I_d+I_r/N} \quad (1)$$

$$H_2O_2\%=200\frac{I_r/N}{I_d+I_r/N} \quad (2)$$

3. Results and Discussion

Following the schematic in Fig.1, B,N@C catalysts were obtained from boron species@ZIF-8 (B@ZIF-8) composites. Similar to N@C, B,N@C-AB and B,N@C-BA display only two XRD (Fig. S1) peaks but with much higher intensity at 25.1° and 43.3°, which can be assigned to (002) and (100) of the graphitic carbon. The higher intensity demonstrates that B doping significantly improves crystallinity. Raman spectra (Fig. S2) can be deconvoluted into four types of carbon configurations at 1336 (D_1), 1186 (D_2), 1501 (D_3), and 1592 (G) cm^{-1}, respectively. The D_1 band is ascribed to the defects and disorders in the carbon while the G band corresponds to the ordered sp^2 bonded graphite carbon. The lower I_{D1}/I_G value (1.97 and 1.91) of B,N@C than N@C (2.12), as shown in Fig. S3, indicates a higher degree of structural graphitization, which is in agreement with the XRD results.

Fig. 2a and Fig. S4 present TEM and SEM images of the ZIF-8 host, respectively. The rhombic dodecahedral host has an average particle size of 150 nm, with a PXRD pattern matching the simulated pattern of ZIF-8 single-crystal (Fig. S5). To prepare B@ZIF-8 hybrids, AB or BA was applied as guest molecules to embed boron species into ZIFs by a DSI method. Given the spherical pore size of the ZIF-8 host (cavity diameter ≈11.6 Å and window (channel) diameter ≈ 3.4 Å) [51, 52], both AB (size ⩽ 3.2 Å) and BA (size ⩽ 3.3 Å) can be confined within the pores of ZIF-8 (Fig. S6). BA ($B(OH)_3$) is one of the most used molecules for B doping [53-57]. However, it has limited solubility in water (0.9 mol/L), which results in limited loading efficiency [58, 59]. In comparison, AB (NH_3BH_3), the simplest B-N compound

has a high solubility in many solvents [60]. The solubility limit of AB in water is 11.4 mol/L [61], nearly 13 times that of BA. Therefore, to introduce 0.32 mmol of B into ZIF-8 hosts in this study, the impregnation process using BA aqueous solution (0.8 mol/L) was repeated four times, while one impregnation was sufficient using AB aqueous solution (3.2 mol/L).

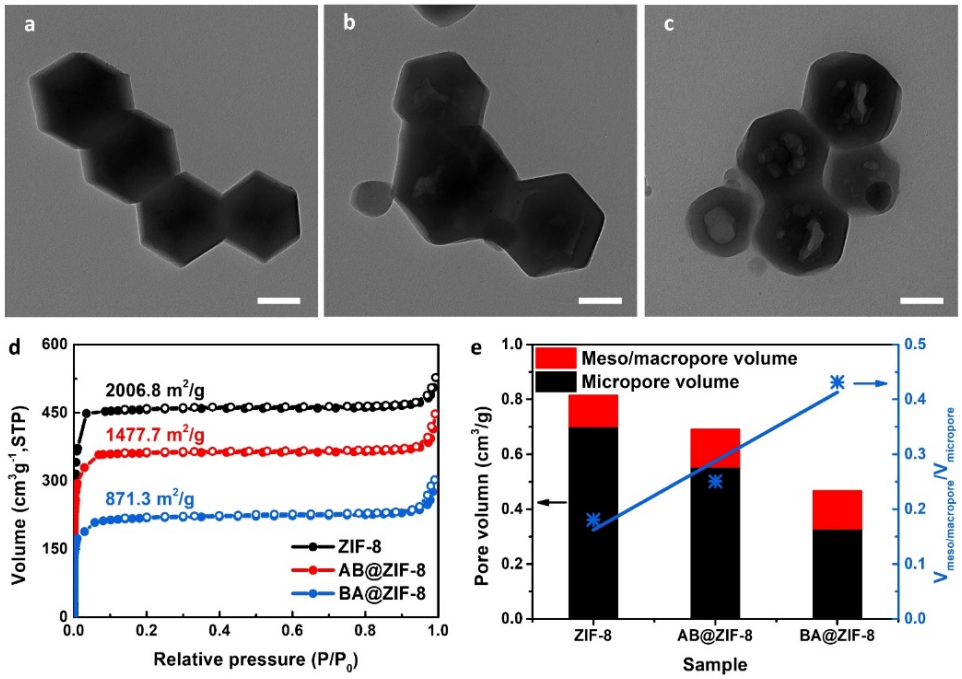

Fig. 2. Characterization of ZIF-8 and B@ZIF-8 composites. TEM images of (a) ZIF-8, (b) AB@ZIF-8, and (c) BA@ZIF-8. All scale bars are 100 nm. (d) N_2 sorption isotherms at -196 °C, and (e) their corresponding pore volume.

When the AB or BA aqueous solution was added dropwise into cyclohexane suspension of ZIF-8, the dispersed aqueous droplets containing the guest molecules could completely diffuse into the hydrophilic pores in ZIF, rather than deposit on the out surface of ZIF-8 hosts, which is based on the immiscibility between water and cyclohexane. As a result, the morphologies of B@ZIF-8 composites stay similar to that of ZIF-8, as shown by SEM images (Fig. S7, 8). AB@ZIF-8 and BA@ZIF-8 composites also display PXRD patterns similar to that of the parent ZIF-8 (Fig. S9). This indicates that there are no appreciable

structural changes in ZIF-8 upon encapsulation of guest molecules in the pores of the host. No diffractions were detected for AB and BA in B@ZIF-8 composite, indicating that B species are distributed in a disordered way. Nevertheless, because of its sensitivity to the aqueous solution, especially acidic solution, the host ZIF-8, which is predominantly microporous, was etched and converted into structures with larger pores after impregnation, confirmed by TEM images of AB@ZIF-8 and BA@ZIF-8 composites (Fig. 2b, c).

AB hydrolyzes slowly in a water-based solution upon the following equation: $NH_3BH_3 + 4\ H_2O \rightarrow NH_4^+ + B(OH)_4^- + 3\ H_2$. After three hours in water, AB remained quite stable without obvious hydrolysis when checked using solution ^{11}B nuclear magnetic resonance (NMR) (Fig. S10). Fourier transform infrared (FTIR) spectroscopy (Fig. S11, S12) also show that AB and BA were loaded into ZIF-8 because the FTIR spectra of AB@ZIF-8 and BA@ZF-8 exhibit multiple bonds which are combinations of those observed in the ZIF-8 and the AB or BA spectra. Notably, some new bands of AB@ZIF-8 at around 3307 and 2323 cm^{-1} could be attributed to the N-H stretch and B-H stretch modes, respectively [62]. So it is believed that AB and BA have diffused into the pores of ZIF-8.

The etching inside the ZIF-8 host is due to the protons produced by hydrolysis of impregnated AB and BA. We collected solid-state ^{11}B NMR spectra (Fig. S13) to identify the B species presented in the AB@ZIF-8 and BA@ZIF-8 composites. The signal at 15.7 ppm for BA@ZIF-8 composite can be ascribed to BO_3 group [63, 64], while the one at 1.8 ppm is related to BO_4 [63, 65], produced by the equilibrium $B(OH)_3 + H_2O \rightleftharpoons B(OH)_4^- + H^+$. The spectrum of the AB@ZIF-8 composite is similar to that of BA@ZIF-8 but features a much weaker peak at −20 ppm, suggesting that AB hydrolyzes predominately to $B(OH)_4^-$. The overall reaction can be written as $NH_3BH_3 + 4\ H_2O \rightarrow NH_4^+ + B(OH)_4^- + 3\ H_2$, instead of $NH_3BH_3 + 3\ H_2O \rightarrow NH_3 + B(OH)_3 + 3\ H_2$ [61]. Therefore, the fewer protons in the case of AB@ZIF-8 resulted in a milder etching of the pores inside ZIF-8. This is corroborated by the change in surface area as can be seen in the N_2 adsorption-desorption isotherms (Fig. 2d). Compared with the ZIF-8 hosts, both AB@ZIF-8 and BA@ZIF-8 exhibit a decreased surface area. BA@ZIF-8 has the

smallest one, which is due to the enlargement of the pores and channels within the ZIF-8 host by BA etching. All three samples showed a steep increase in nitrogen uptake at lower p/p_0 indicating a high ratio of micropores. AB@ZIF-8 and BA@ZIF-8 composites showed a slight increase in N_2 uptake at a higher p/p_0 ratio ($p/p_0 > 0.95$) with a hysteresis loop indicating the presence of more mesopores and macropores than in ZIF-8. The corresponding decrease in the nitrogen uptake ($p/p_0 < 0.1$) for AB@ZIF-8 and BA@ZIF-8 indicated that the adsorption occurred mainly into the micropores [66, 67]. Pore size distribution was analyzed based upon non-local density functional theory (NL-DFT) calculations (Fig. S14). Consistent with the decreased nitrogen uptake (p/p0 < 0.1), the micropore size decreased from 1.17 nm for ZIF-8 to 1.09 nm for AB@ZIF-8 and 1.00 nm for BA@ZIF-8. The microporous volume (Fig. 2e) decreased from 0.69 cm^3g^{-1} for ZIF-8 to 0.55 cm^3g^{-1} for AB@ZIF-8 and 0.33cm^3g^{-1} for BA@ZIF-8. AB@ZIF-8 and BA@ZIF-8 have larger meso- and macroporous volumes (0.13 cm^3g^{-1} and 0.14 cm^3g^{-1}, respectively) than ZIF-8 (0.12 cm^3g^{-1}). The decrease in microporous volume, increase in mesoporous volume and the corresponding increase in the ratio of meso/macropore to micropore volume (0.18 for ZIF-8, 0.25 for AB@ZIF-8 and 0.43 for BA@ZIF-8) are all due to the etching of the ZIF-8 host.

The change in microstructure after impregnation has a direct impact on the microstructure of B,N@C obtained by pyrolyzing these ZIF-8 precursors. After pyrolysis in N_2, AB@ZIF-8 and BA@ZIF-8 composite were converted into hierarchical porous carbon frameworks with uniform B and N co-doping, denoted as B,N@C-AB and B,N@C-BA, respectively. SEM characterizations reveal that the resultant materials inherit the morphology of N@C precursors with a mean diameter of 80 nm (Fig. S15, S16, S17). TEM and AC HAADF-STEM images reveal that compared with N@C (Fig. 3a), B,N@C-AB features larger pores in its hierarchical porous structures (Fig. 3b, d) while B,N@C-BA displays hollow space inside (Fig. 3c). These observations clearly indicate a correlation in structure between the B doped ZIF-8 and the resultant B,N@C. The elemental mapping analysis of B,N@C-AB demonstrates that B and N are uniformly distributed in the entire carbon matrix (Fig. 3e).

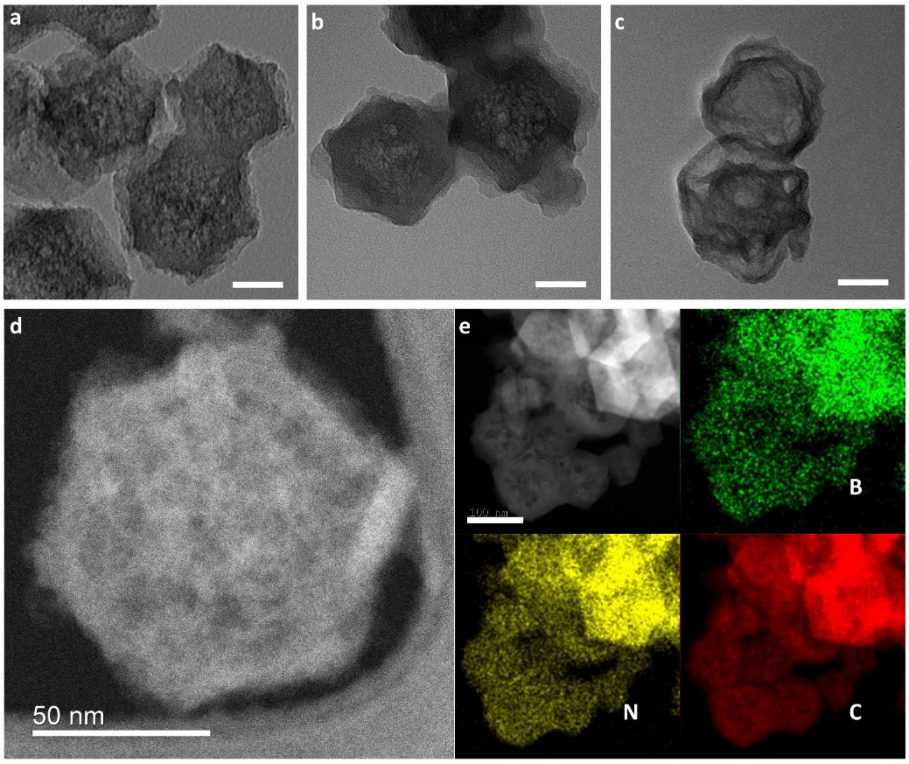

Fig. 3. Characterization of N@C and B,N@Cs. TEM images of (a) N@C, (b) B,N@C-AB, and (c) B,N@C-BA. All scale bars are 50 nm. (d) Aberration corrected HAADF-STEM, and (e) EDS mapping of B,N@C-AB, with the scale bar being 100 nm.

XPS analyses were carried out to expound the bonding contributions. B contents in B,N@C-AB and B,N@C-BA are 15.0 and 16.9 at %, respectively (Fig. S18). The contents of N in B,N@C (14.4 at% for B,N@C-AB and 13.2 at% for B,N@C-BA) are much higher than 9.4 at% in N@C (Fig. S18). These results demonstrate that B is beneficial in preventing N loss during the heat treatment due to the formation of B-N (Fig. 4a) [68]. High-resolution XPS spectra reveal the existence of multiple types of B dopants in the materials. The B 1s peaks can be deconvoluted into three peaks at 190.6, 191.9, and 192.5 eV, which can be assigned to B-C, B-N, and B-O, respectively (Fig. 4a). B-B peaks (at 187.8 and 189.1 eV [69]) are invisible for all the B,N@C samples, indicating B atoms embedded in the carbon skeleton as single atoms. Similarly, the N 1s peak can be deconvoluted into peaks at 397.8, 398.4, 399.5, 400.7, and 402.4 eV, which are associated with N-B, pyridinic (N6), pyrrolic (N5), quaternary N (NQ), and oxidic N atoms, respectively (Fig. 4b) [39, 40]. C 1s spectra display four peaks centered at ca. 284.4, 284.8, 285.9,

and 288.5 eV after deconvolution, which can be assigned to C-B, C-C, C-N, and C=O, respectively (Fig. S19) [27, 56]. Peak fitting was performed to determine the composition of each type of dopant (Fig. 4c). For B,N@C-AB, approximately 4.7 at% B is in the form of B-C, and 4.9 at% B is in the form of B-N. In comparison, there are slightly more B-C (5.3 at%) and less B-N (4.1 at%) in B,N@C-BA. Consistently, about 2.2 at% and 1.8 at% N in B,N@C-AB and B,N@C-BA are in the form of N-B, respectively. These results indicate that there is about twice as many B as N in the B-N motif, meaning a B:N ratio of 2:1. The introduction of B helps with the retainment of N by forming B-N during pyrolysis. The co-existence of B and N breaks the electroneutrality of the carbon matrix due to the electronegativity difference between B, N and C, producing not only C^+ but also B^+ for O_2 adsorption that improves the ORR activity [25, 70, 71].

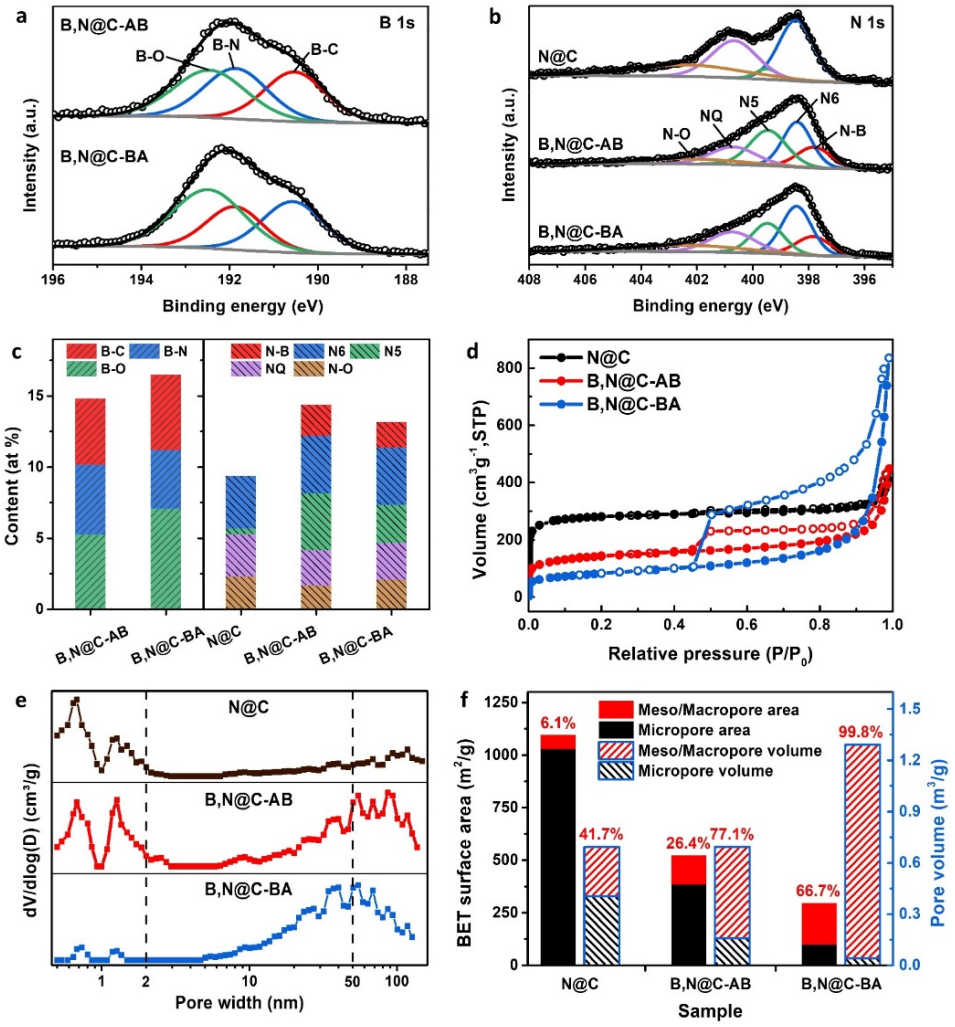

Fig. 4. Characterization of N@C and B,N@Cs. The high-resolution XPS spectra of (a) B 1 s, (b) N 1 s of N@C and B,N@C samples. (c) The contents of B and N determined by fitting the XPS spectra. (d) N_2 sorption isotherms at -196 °C, and (e) their corresponding pore size distributions (PSD) calculated using NL-DFT method, and (f) BET surface areas and pore volumes.

Samples derived from ZIF-8 and B@ZIF-8s exhibited different N_2 sorption isotherms (Fig. 4d), indicating different porous structures (Fig. 4e). N@C shows a reversible type I isotherm which is typical for microporous samples. B,N@C-BA shows a type IV isotherm featuring a broad hysteresis loop and a steep increase of the N_2 uptake at p/p_0 close to 1, suggesting meso/macropores-dominated structure. B,N@C-AB exhibited combined characteristics of type I and IV isotherms, which is due to the existence of pore sizes spanning from micro- to macropores (Fig. 4e). As a result, B,N@C-AB has a larger BET

surface area of 523.0 m^2g^{-1} but a smaller pore volume of 0.69 m^3g^{-1} than B,N@C-BA (295.3 m^2g^{-1} and 1.29 m^3g^{-1}). Furthermore, the proportion of meso/macroporous surface areas and volumes of B,N@C-AB and B,N@C-BA are all higher than those of N@C (Fig. 4f). The relatively high surface of B,N@Cs and their hierarchical porous structure with considerable amounts of meso/macropores, would be favorable for the accessibility of electrolytes and exposing more active sites for oxygen reduction.

To examine the influence of boron on catalytic performance, the ORR activities of the N@C and B,N@C catalysts were first evaluated by cyclic voltammogram (CV) tests in N_2- and O_2-saturated electrolyte (0.1 M KOH) at a scan rate of 10 mV s^{-1} (Fig. 5a). All the samples showed no redox peaks in the N_2-saturated medium, but distinct cathodic peaks appeared in all the cases with the O_2-saturated electrolyte, which can be ascribed to oxygen reduction. The B,N@C-AB showed a peak at 900 mV, which is higher than N@C (786 mV) and B,N@C-BA (841 mV), demonstrating the best oxygen reduction activity. As shown in Fig. 4c, all the samples have similar amounts of N6 (3.7 at% for N@C, 4.0 at% for B,N@C-AB, and 4.0 at% for B,N@C-BA), which are known to lower the overpotential in ORR [72, 73]. Therefore, other factors such as boron doping and structures cause the difference in ORR performance. Rotating ring-disc electrode (RRDE) measurements were carried out to compare the electrocatalytic ORR activities and determine the electron transfer numbers over different catalysts in alkaline (0.1M KOH) solution. The ORR linear sweep voltammogram (LSV) polarization curves of different catalysts in RRDE were recorded in O_2-saturated 0.1 M KOH solution at a rotation rate of 1600 rpm, with commercial Pt/C catalyst as a comparison (Fig. 5b) and with the H_2O_2 currents detected by the Pt ring (Fig. S20).

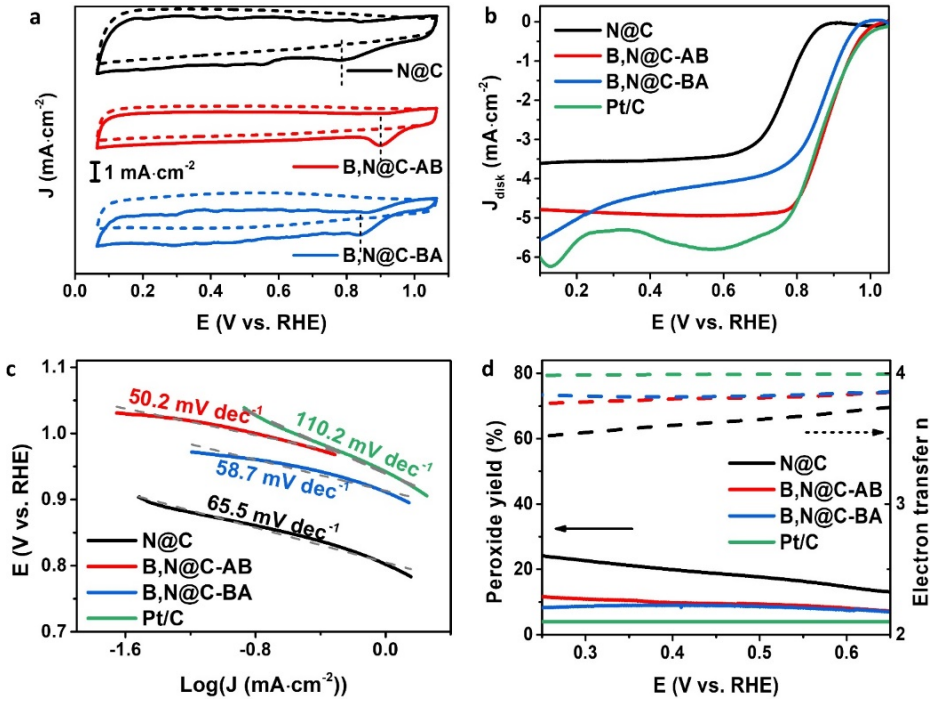

Fig. 5. Electrocatalytic performance for ORR in 0.1 M KOH electrolyte. (a) CV curves in N_2-saturated (dotted lines) and O_2-saturated (solid lines) alkaline electrolytes. (b) LSV curves with a fixed rotation rate of 1600 rpm at 10 mV s^{-1}. (c) Tafel plots and (d) electron transfer number and H_2O_2 selectivity derived from LSV curves.

In agreement with the CV observations, B,N@C-AB shows an exceedingly high ORR activity with the most positive half-wave potential ($E_{1/2}$) of 887 mV, which is much better than that of the N@C ($E_{1/2}$ = 767 mV) and also comparable to that of commercial Pt/C ($E_{1/2}$ = 859 mV). B,N@C-BA also exhibits a relatively high $E_{1/2}$ of 840 mV. Both B,N@C samples show larger diffusion-limited current density (DLCD = 4.79 mA·cm^{-2} for B,N@C-AB, 5.55 mA·cm^{-2} for B,N@C-BA) than N@C (3.61 mA·cm^{-2}), which indicates that meso- and macropores are beneficial for mass transfer [12, 74]. The performance of B,N@C frameworks is on par or even better than reported metal-free BCN catalysts (Table S1).

Tafel plots of N@C, B,N@C-AB, B,N@C-BA and commercial Pt/C are displayed in Fig. 5c. The B,N@C-AB displays a lower Tafel slope than those of N@C and B,N@C-BA, further manifesting that the B,N@C-AB catalyst exhibits the fastest kinetics toward ORR. The H_2O_2 molar yields and electron transfer numbers calculated based on the corresponding disk and ring currents are both plotted in Fig. 5d.

The H_2O_2 yields of B,N@C-AB and B,N@C-BA are below 12% from 0.2 V to 0.7 V with electron transfer numbers larger than 3.75, indicating a strong catalytic effect in converting O_2 to O^{2-} via a four-electron pathway. Much higher H_2O_2 yield and smaller electron transfer number were observed on N@C, indicating its lower-efficiency $4e^-$ pathway in ORR. The high ORR activities of B,N@C are likely due to two key factors: (1) the electronic structure of the catalysts is optimized by high boron doping, which promotes the adsorption of the *OH and *OOH intermediates at the B sites [70]; (2) the etching caused by boron species in ZIF-8 generates meso- and macroporous structure which exposes more active sites and contributes to better mass transfer.

4. Conclusions

In summary, we have developed an effective method for the fabrication of B and N co-doped hierarchical porous carbon frameworks. The key step in the fabrication is the introduction of boron species into ZIF precursors via an integrated double-solvent impregnation and confined-etching. The encapsulation of boron-containing guests in the ZIF-8 pores plays an important role in achieving a uniform and dense doping of B atoms in the N@C frameworks and inducing the hierarchical micro/meso/macro multimodal porosities. The excellent electrochemical ORR performance of B,N@Cs could be associated with their hierarchical porous structures that contribute to mass transfer and exposure of active sites, as well as abundant reactive sites due to the high level of boron doping. This integrated method of impregnation and confined etching is applicable to fabricate complex nanoarchitectures with desired pore sizes and pore volume, which will be beneficial for various catalytic reactions.

Acknowledgements

We acknowledge support under the Australian Research Council's Future Fellowship (project number: FT190100658, Z.H.) and support from the Alexander von Humboldt Foundation (Z.H.). X.W. also acknowledges the Chinese Scholarship Council (CSC) for financial support.

References

[1] H. Xing, Y. Zhang, J. Hu, R. Krishna, L. Wang, L. Yang, X. Cui, S. Duttwyler; Rational design of microporous MOFs with anionic boron cluster functionality and cooperative dihydrogen binding sites for highly selective capture of acetylene. Angew. Chem. Int. Ed. **2020**.

[2] L. Sun, Y. Yuan, F. Wang, Y. Zhao, W. Zhan, X. Han; Selective wet-chemical etching to create TiO_2@MOF frame heterostructure for efficient photocatalytic hydrogen evolution. Nano Energy. **2020**, 74, 104909.

[3] X.-C. Xie, K.-J. Huang, X. Wu; Metal–organic framework derived hollow materials for electrochemical energy storage. J. Mater. Chem. A. **2018**, 6, 6754-6771.

[4] J. Liu, D. Zhu, C. Guo, A. Vasileff, S.-Z. Qiao; Design strategies toward advanced MOF-derived electrocatalysts for energy-conversion reactions. Adv. Energy Mater. **2017**, 7, 1700518.

[5] C. Wang, J. Kim, J. Tang, M. Kim, H. Lim, V. Malgras, J. You, Q. Xu, J. Li, Y. Yamauchi; New strategies for novel MOF-derived carbon materials based on nanoarchitectures. Chem. **2020**, 6, 19-40.

[6] X. Song, Y. Jiang, F. Cheng, J. Earnshaw, J. Na, X. Li, Y. Yamauchi; Hollow carbon-based nanoarchitectures based on ZIF: Inward/outward contraction mechanism and beyond. Small. **2020**, 17, 2004142.

[7] K. Zhang, H. Hu, L. Shi, B. Jia, H. Huang, X. Han, X. Sun, T. Ma; Strategies for optimizing the photocatalytic water-splitting performance of metal–organic framework-based materials. Small Sci. **2021**, 1, 2100060.

[8] K. Wang, C. Wu, F. Wang, G. Jiang; MOF-derived copx nanoparticles embedded in nitrogen-doped porous carbon polyhedrons for nanomolar sensing of p-nitrophenol. ACS Appl. Nano Mater. **2018**, 1, 5843-5853.

[9] F. Pan, H. Zhang, K. Liu, D. Cullen, K. More, M. Wang, Z. Feng, G. Wang, G. Wu, Y. Li; Unveiling active sites of CO_2 reduction on nitrogen-coordinated and atomically dispersed iron and cobalt catalysts. ACS Catal. **2018**, 8, 3116-3122.

[10] W. Xia, J. Zhu, W. Guo, L. An, D. Xia, R. Zou; Well-defined carbon polyhedrons prepared from nano metal–organic frameworks for oxygen reduction. J. Mater. Chem. A. **2014**, 2, 11606-11613.

[11] Z.-X. Cai, Z.-L. Wang, Y.-J. Xia, H. Lim, W. Zhou, A. Taniguchi, M. Ohtani, K. Kobiro, T. Fujita, Y. Yamauchi; Tailored catalytic nanoframes from metal–organic frameworks by anisotropic surface modification and etching for the hydrogen evolution reaction. Angew. Chem. Int. Ed. **2021**, 60, 4747-4755.

[12] Z. Zhu, H. Yin, Y. Wang, C.-H. Chuang, L. Xing, M. Dong, Y.-R. Lu, G. Casillas-Garcia, Y. Zheng, S. Chen, et al.; Coexisting single-atomic Fe and Ni sites on hierarchically ordered porous carbon as a highly efficient orr electrocatalyst. Adv. Mater. **2020**, 32, 2004670.

[13] Y. Fang, X. Wang; Metal-free boron-containing heterogeneous catalysts. Angew. Chem. Int. Ed. **2017**, 56, 15506-15518.

[14] Z. Li, Y. Chen, T. Ma, Y. Jiang, J. Chen, H. Pan, W. Sun; 2D metal-free nanomaterials beyond graphene and its analogues toward electrocatalysis applications. Adv. Energy Mater. **2021**, 11, 2101202.

[15] J. Wu, X. Zheng, C. Jin, J. Tian, R. Yang; Ternary doping of phosphorus, nitrogen, and sulfur into porous carbon for enhancing electrocatalytic oxygen reduction. Carbon. **2015**, 92, 327-338.

[16] S. Zhao, J. Liu, C. Li, W. Ji, M. Yang, H. Huang, Y. Liu, Z. Kang; Tunable ternary (N, P, B)-doped porous nanocarbons and their catalytic properties for oxygen reduction reaction. ACS Appl. Mater. Interfaces. **2014**, 6, 22297-22304.

[17] P. Huang, H. Li, X. Huang, D. Chen; Multiheteroatom-doped porous carbon catalyst for oxygen reduction reaction prepared using 3D network of ZIF-8/polymeric nanofiber as a facile-doping template. ACS Appl. Mater. Interfaces. **2017**, 9, 21083-21088.

[18] C.N.R. Rao, M. Chhetri; Borocarbonitrides as metal-free catalysts for the hydrogen evolution reaction. Adv. Mater. **2019**, 31, 1803668.

[19] M. Zheng, J. Shi, T. Yuan, X. Wang; Metal-free dehydrogenation of n-heterocycles by ternary h -bcn nanosheets with visible light. Angewandte Chemie. **2018**, 130, 5585-5589.

[20] C.N.R. Rao, K. Gopalakrishnan; Borocarbonitrides, $B_xC_yN_z$: Synthesis, characterization, and properties with potential applications. ACS Appl. Mater. Interfaces. **2017**, 9, 19478-19494.

[21] S. Wang , E. Iyyamperumal , A. Roy, Y. Xue, D. Yu, L. Dai; Vertically aligned BCN nanotubes as efficient metal-free electrocatalysts for the oxygen reduction reaction: A synergetic effect by co-doping with boron and nitrogen. Angew. Chem. Int. Ed. **2011**, 50, 11756-11760.

[22] Y. Hao, S. Wang, Y. Shao, Y. Wu, S. Miao; High-energy density Li-ion capacitor with layered SnS_2/reduced graphene oxide anode and BCN nanosheet cathode. Adv. Energy Mater. **2020**, 10, 1902836.

[23] W. Lei, S. Qin, D. Liu, D. Portehault, Z. Liu, Y. Chen; Large scale boron carbon nitride nanosheets with enhanced lithium storage capabilities. Chem. Commun. **2013**, 49, 352-354.

[24] R. Nandan, G.K. Goswami, K.K. Nanda; Direct synthesis of Pt-free catalyst on gas diffusion layer of fuel cell and usage of high boiling point fuels for efficient utilization of waste heat. Appl. Energy. **2017**, 205, 1050-1058.

[25] Y. Zheng, Y. Jiao, L. Ge, M. Jaroniec, S.Z. Qiao; Two-step boron and nitrogen doping in graphene for enhanced synergistic catalysis. Angew. Chem. Int. Ed. **2013**, 52, 3110-3116.

[26] S. Wang, L. Zhang, Z. Xia, A. Roy, D.W. Chang, J.-B. Baek, L. Dai; BCN graphene as efficient metal-free electrocatalyst for the oxygen reduction reaction. Angew. Chem. Int. Ed. **2012**, 51, 4209-4212.

[27] M. Chhetri, S. Maitra, H. Chakraborty, U.V. Waghmare, C.N.R. Rao; Superior performance of borocarbonitrides, $B_xC_yN_z$, as stable, low-cost metal-free electrocatalysts for the hydrogen evolution reaction. Energy Environ. Sci. **2016**, 9, 95-101.

[28] H.-W. Zhang, Y.-Y. Li, W.-Q. Huang, B.-X. Zhou, S.-F. Ma, Y.-X. Lu, A.-L. Pan, G.-F. Huang; Hollow BCN microrods with hierarchical multichannel structure as a multifunctional material: Synergistic effects of structural topology and composition. Carbon. **2019**, 148, 231-240.

[29] D. Shi, B. Chang, Z. Ai, H. Jiang, F. Chen, Y. Shao, J. Shen, Y. Wu, X. Hao; Boron carbonitride with tunable B/N lewis acid/base sites for enhanced electrocatalytic overall water splitting. Nanoscale. **2021**, 13, 2849-2854.

[30] C. Chen, D. Yan, Y. Wang, Y. Zhou, Y. Zou, Y. Li, S. Wang; B-N pairs enriched defective carbon nanosheets for ammonia synthesis with high efficiency. Small. **2019**, 15, 1805029.

[31] Q. Geng, G. Huang, Y. Liu, Y. Li, L. Liu, X. Yang, Q. Wang, C. Zhang; Facile synthesis of B/N co-doped 2D porous carbon nanosheets derived from ammonium humate for supercapacitor electrodes. Electrochim. Acta. **2019**, 298, 1-13.

[32] S. Wang, F. Ma, H. Jiang, Y. Shao, Y. Wu, X. Hao; Band gap-tunable porous borocarbonitride nanosheets for high energy-density supercapacitors. ACS Appl. Mater. Interfaces. **2018**, 10, 19588-19597.

[33] M.-R. Liu, Q.-L. Hong, Q.-H. Li, Y. Du, H.-X. Zhang, S. Chen, T. Zhou, J. Zhang; Cobalt boron imidazolate framework derived cobalt nanoparticles encapsulated in B/N codoped nanocarbon as efficient bifunctional electrocatalysts for overall water splitting. Adv. Funct. Mater. **2018**, 28, 1801136.

[34] Y. Qian, Z. Hu, X. Ge, S. Yang, Y. Peng, Z. Kang, Z. Liu, J.Y. Lee, D. Zhao; A metal-free ORR/OER bifunctional electrocatalyst derived from metal-organic frameworks for rechargeable zn-air batteries. Carbon. **2017**, 111, 641-650.

[35] X. Chen, Y. Xie, Y. Shao, K. Shen, Y. Li; Facile synthesis of boron and nitrogen dual-doped hollow mesoporous carbons for efficient reduction of 4-nitrophenol. ACS Appl. Mater. Interfaces. **2021**, 13, 42598-42604.

[36] C. Van Nguyen, S. Lee, Y.G. Chung, W.-H. Chiang, K.C.W. Wu; Synergistic effect of metal-organic framework-derived boron and nitrogen heteroatom-doped three-dimensional porous carbons for precious-metal-free catalytic reduction of nitroarenes. Appl. Catal., B. **2019**, 257, 117888.

[37] Y. Li, H. Xu, H. Huang, L. Gao, Y. Zhao, T. Ma; Synthesis of Co–B in porous carbon using a metal–organic framework (MOF) precursor: A highly efficient catalyst for the oxygen evolution reaction. Electrochem. Commun. **2018**, 86, 140-144.

[38] H. Tabassum, A. Mahmood, Q. Wang, W. Xia, Z. Liang, B. Qiu, R. zhao, R. Zou; Hierarchical cobalt hydroxide and B/N co-doped graphene nanohybrids derived from metal-organic frameworks for high energy density asymmetric supercapacitors. Sci. Rep. **2017**, 7, 43084.

[39] H. Tabassum, W. Guo, W. Meng, A. Mahmood, R. Zhao, Q. Wang, R. Zou; Metal–organic frameworks derived cobalt phosphide architecture encapsulated into B/N co-doped graphene nanotubes for all ph value electrochemical hydrogen evolution. Adv. Energy Mater. **2017**, 7, 1601671.

[40] H. Zhang, Z. Ma, J. Duan, H. Liu, G. Liu, T. Wang, K. Chang, M. Li, L. Shi, X. Meng, et al.; Active sites implanted carbon cages in core–shell architecture: Highly active and durable electrocatalyst for hydrogen evolution reaction. ACS Nano. **2016**, 10, 684-694.

[41] X. Wei, N. Li, X. Zhang; Co/CoO/C@B three-phase composite derived from ZIF67 modified with $NaBH_4$ solution as the electrocatalyst for efficient oxygen evolution. Electrochim. Acta. **2018**, 264, 36-45.

[42] M.A. Ahsan, T. He, K. Eid, A.M. Abdullah, M.F. Sanad, A. Aldalbahi, B. Alvarado-Tenorio, A. Du, A.R. Puente Santiago, J.C. Noveron; Controlling the interfacial charge polarization of MOF-derived 0D–2D vdw architectures as a unique strategy for bifunctional oxygen electrocatalysis. ACS Appl. Mater. Interfaces. **2022**, 14, 3919-3929.

[43] Y. Wan, W. Zhang, X. Han, L. Zhou, H. Zhen, C. Wu, Q. Yu, G. Xiu; B,N-decorated carbocatalyst based on Fe-MOF/bn as an efficient peroxymonosulfate activator for bisphenol a degradation. J. Hazard. Mater. **2022**, 430, 127832.

[44] C. Tang, B.-Q. Li, Q. Zhang, L. Zhu, H.-F. Wang, J.-L. Shi, F. Wei; Cao-templated growth of hierarchical porous graphene for high-power lithium–sulfur battery applications. Adv. Funct. Mater. **2016**, 26, 577-585.

[45] C.L. Hobday, C.H. Woodall, M.J. Lennox, M. Frost, K. Kamenev, T. Düren, C.A. Morrison, S.A. Moggach; Understanding the adsorption process in ZIF-8 using high pressure crystallography and computational modelling. Nat. Commun. **2018**, 9, 1429.

[46] J. Wang, Z. Huang, W. Liu, C. Chang, H. Tang, Z. Li, W. Chen, C. Jia, T. Yao, S. Wei, et al.; Design of N-coordinated dual-metal sites: A stable and active Pt-free catalyst for acidic oxygen reduction reaction. J. Am. Chem. Soc. **2017**, 139, 17281-17284.

[47] Y.-H. Zhou, X. Cao, J. Ning, C. Ji, Y. Cheng, J. Gu; Pd-doped Cu nanoparticles confined by ZIF-67@ZIF-8 for efficient dehydrogenation of ammonia borane. Int. J. Hydrogen Energy. **2020**, 45, 31440-31451.

[48] Z. Wang, B. Zhang, C. Ye, L. Chen; Recovery of Au(iii) from leach solutions using thiourea functionalized zeolitic imidazolate frameworks (TU*ZIF-8). Hydrometallurgy. **2018**, 180, 262-270.

[49] F. Chang, P. Su, U. Guharoy, R. Ye, Y. Ma, H. Zheng, Y. Jia, J. Liu; Edge-enriched n, s co-doped hierarchical porous carbon for oxygen reduction reaction. Chin. Chem. Lett. **2022**.

[50] J.V. Morabito, L.-Y. Chou, Z. Li, C.M. Manna, C.A. Petroff, R.J. Kyada, J.M. Palomba, J.A. Byers, C.-K. Tsung; Molecular encapsulation beyond the aperture size limit through dissociative linker exchange in metal–organic framework crystals. J. Am. Chem. Soc. **2014**, 136, 12540-12543.

[51] O. Basu, S. Mukhopadhyay, A. De, A. Das, S.K. Das; Tuning the electrochemical and catalytic ORR performance of C_{60} by its encapsulation in ZIF-8: A solid-state analogue of dilute fullerene solution. Mater. Chem. Front. **2021**, 5, 7654-7665.

[52] M. Gutiérrez, C. Martín, M. Van der Auweraer, J. Hofkens, J.-C. Tan; Electroluminescent guest@MOF nanoparticles for thin film optoelectronics and solid-state lighting. Adv. Opt. Mater. **2020**, 8, 2000670.

[53] Y. Xia, X. Zhao, C. Xia, Z.-Y. Wu, P. Zhu, J.Y. Kim, X. Bai, G. Gao, Y. Hu, J. Zhong, et al.; Highly active and selective oxygen reduction to H_2O_2 on boron-doped carbon for high production rates. Nat. Commun. **2021**, 12, 4225.

[54] J. Wang, H. Li, S. Liu, Y. Hu, J. Zhang, M. Xia, Y. Hou, J. Tse, J. Zhang, Y. Zhao; Turning on zn 4s electrons in a N_2-Zn-B_2 configuration to stimulate remarkable ORR performance. Angew. Chem. Int. Ed. **2021**, 60, 181-185.

[55] X. Ma, J. Du, H. Sun, F. Ye, X. Wang, P. Xu, C. Hu, L. Zhang, D. Liu; Boron, nitrogen co-doped carbon with abundant mesopores for efficient CO_2 electroreduction. Appl. Catal., B. **2021**, 298, 120543.

[56] B. Chang, L. Li, D. Shi, H. Jiang, Z. Ai, S. Wang, Y. Shao, J. Shen, Y. Wu, Y. Li, et al.; Metal-free boron carbonitride with tunable boron lewis acid sites for enhanced nitrogen electroreduction to ammonia. Appl. Catal., B. **2021**, 283, 119622.

[57] M.A. Ahsan, T. He, K. Eid, A.M. Abdullah, M.L. Curry, A. Du, A.R. Puente Santiago, L. Echegoyen, J.C. Noveron; Tuning the intermolecular electron transfer of low-dimensional and metal-free BCN/C_{60} electrocatalysts via interfacial defects for efficient hydrogen and oxygen electrochemistry. J. Am. Chem. Soc. **2021**, 143, 1203-1215.

[58] Q.-L. Zhu, W. Xia, T. Akita, R. Zou, Q. Xu; Metal-organic framework-derived honeycomb-like open porous nanostructures as precious-metal-free catalysts for highly efficient oxygen electroreduction. Adv. Mater. **2016**, 28, 6391-6398.

[59] Q.-L. Zhu, W. Xia, L.-R. Zheng, R. Zou, Z. Liu, Q. Xu; Atomically dispersed Fe/N-doped hierarchical carbon architectures derived from a metal–organic framework composite for extremely efficient electrocatalysis. ACS Energy Lett. **2017**, 2, 504-511.

[60] F.H. Stephens, V. Pons, R. Tom Baker; Ammonia–borane: The hydrogen source par excellence? Dalton Trans. **2007**, 25, 2613-2626.

[61] A. Brockman, Y. Zheng, J. Gore; A study of catalytic hydrolysis of concentrated ammonia borane solutions. Int. J. Hydrogen Energy. **2010**, 35, 7350-7356.

[62] U.B. Demirci; Ammonia borane, a material with exceptional properties for chemical hydrogen storage. Int. J. Hydrogen Energy. **2017**, 42, 9978-10013.

[63] C. Huang, M. Mutailipu, F. Zhang, K.J. Griffith, C. Hu, Z. Yang, J.M. Griffin, K.R. Poeppelmeier, S. Pan; Expanding the chemistry of borates with functional $[BO_2]^-$ anions. Nat. Commun. **2021**, 12, 2597.

[64] S. Kroeker, J.F. Stebbins; Three-coordinated boron-11 chemical shifts in borates. Inorg. Chem. **2001**, 40, 6239-6246.

[65] S. Geng, F.U. Shah, P. Liu, O.N. Antzutkin, K. Oksman; Plasticizing and crosslinking effects of borate additives on the structure and properties of poly(vinyl acetate). RSC Adv. **2017**, 7, 7483-7491.

[66] Z. Li, G. Zhu, G. Lu, S. Qiu, X. Yao; Ammonia borane confined by a metal−organic framework for chemical hydrogen storage: Enhancing kinetics and eliminating ammonia. J. Am. Chem. Soc. **2010**, 132, 1490-1491.

[67] Z. Zhang, J. Sun, F. Wang, L. Dai; Efficient oxygen reduction reaction (ORR) catalysts based on single iron atoms dispersed on a hierarchically structured porous carbon framework. Angew. Chem. Int. Ed. **2018**, 57, 9038-9043.

[68] P. Wei, X. Li, Z. He, X. Sun, Q. Liang, Z. Wang, C. Fang, Q. Li, H. Yang, J. Han, et al.; Porous N, B co-doped carbon nanotubes as efficient metal-free electrocatalysts for ORR and Zn-air batteries. Chem. Eng. J. **2021**, 422, 130134.

[69] Q. Li, V.S.C. Kolluru, M.S. Rahn, E. Schwenker, S. Li, R.G. Hennig, P. Darancet, M.K.Y. Chan, M.C. Hersam; Synthesis of borophane polymorphs through hydrogenation of borophene. Science. **2021**, 371, 1143-1148.

[70] X. Li, L. Fan, B. Xu, Y. Shang, M. Li, L. Zhang, S. Liu, Z. Kang, Z. Liu, X. Lu, et al.; Single-atom-like B-N_3 sites in ordered macroporous carbon for efficient oxygen reduction reaction. ACS Appl. Mater. Interfaces. **2021**, 13, 53892-53903.

[71] Y.J. Gong, H.L. Fei, X.L. Zou, W. Zhou, S.B. Yang, G.L. Ye, Z. Liu, Z.W. Peng, J. Lou, R. Vajtai, et al.; Boron- and nitrogen-substituted graphene nanoribbons as efficient catalysts for oxygen reduction reaction. Chem. Mater. **2015**, 27, 1181-1186.

[72] H. Miao, S. Li, Z. Wang, S. Sun, M. Kuang, Z. Liu, J. Yuan; Enhancing the pyridinic N content of nitrogen-doped graphene and improving its catalytic activity for oxygen reduction reaction. Int. J. Hydrogen Energy. **2017**, 42, 28298-28308.

[73] J. Wu, L. Ma, R.M. Yadav, Y. Yang, X. Zhang, R. Vajtai, J. Lou, P.M. Ajayan; Nitrogen-doped graphene with pyridinic dominance as a highly active and stable electrocatalyst for oxygen reduction. ACS Appl. Mater. Interfaces. **2015**, 7, 14763-14769.

[74] T. Wang, Y. He, Y. Liu, F. Guo, X. Li, H. Chen, H. Li, Z. Lin; A ZIF-triggered rapid polymerization of dopamine renders Co/N-codoped cage-in-cage porous carbon for highly efficient oxygen reduction and evolution. Nano Energy. **2021**, 79, 105487.

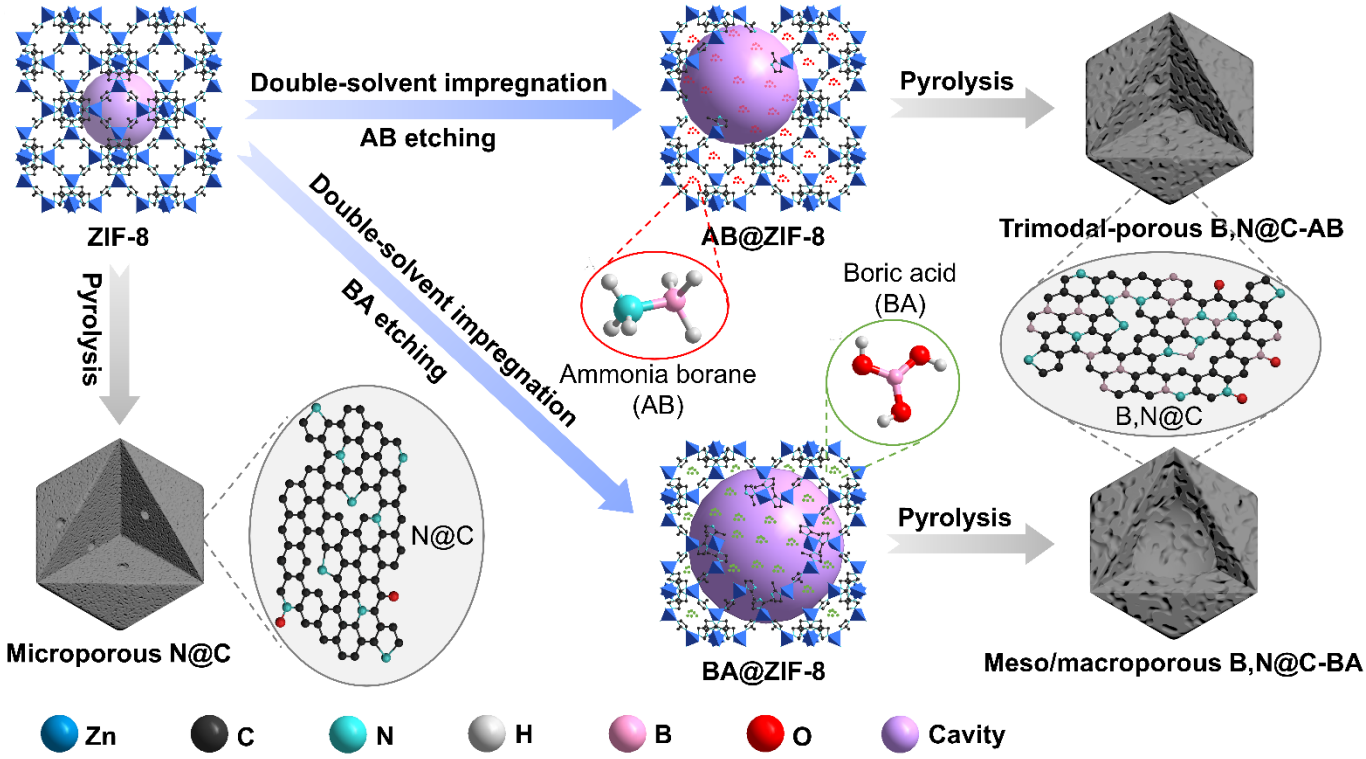

Fig. 1. Schematic diagram of the fabrication of B,N@C nanomaterials.

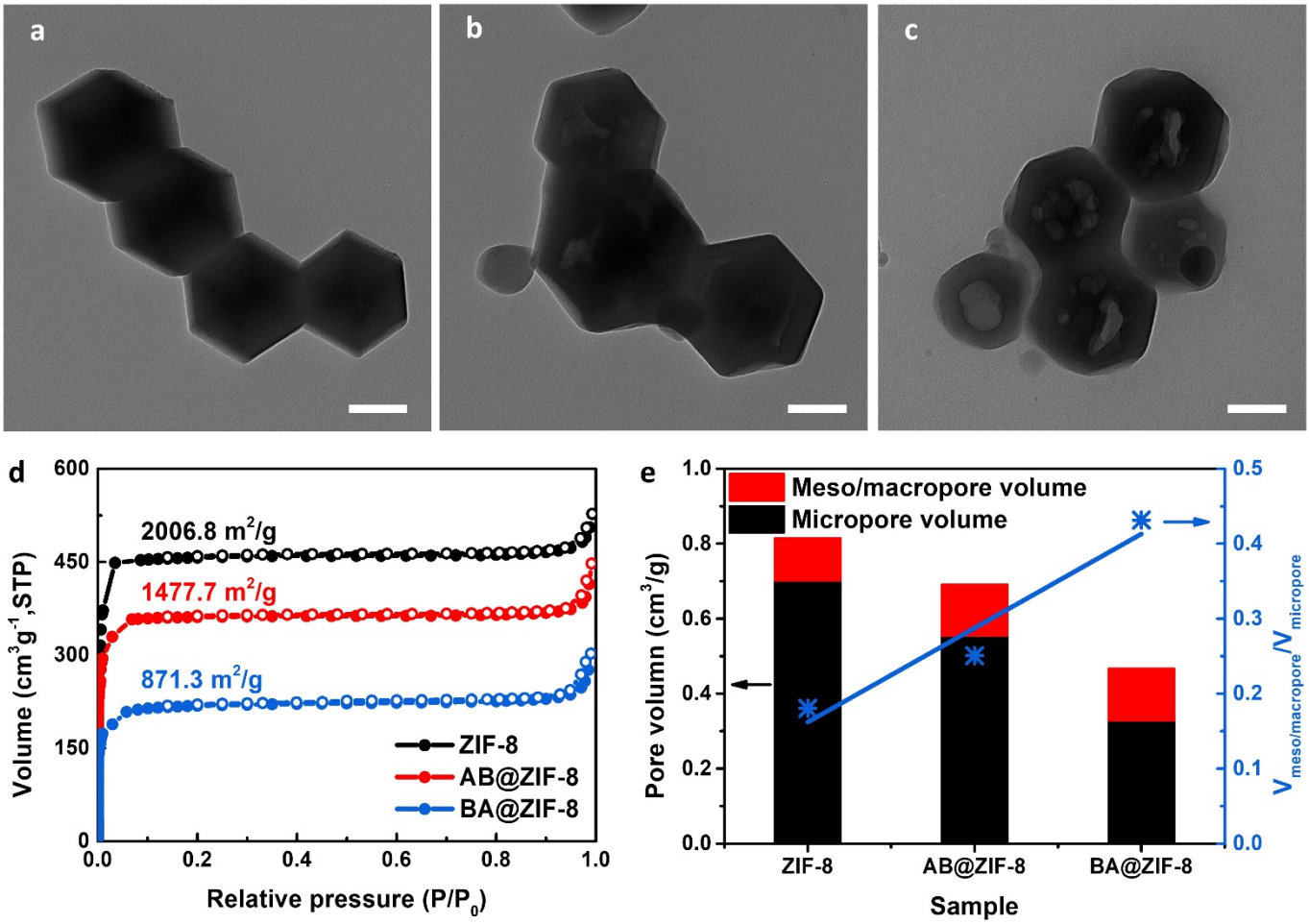

Fig. 2. Characterization of ZIF-8 and B@ZIF-8 composites. TEM images of (a) ZIF-8, (b) AB@ZIF-8, and (c) BA@ZIF-8. All scale bars are 100 nm. (d) N_2 sorption isotherms at -196 °C, and (e) their corresponding pore volume.

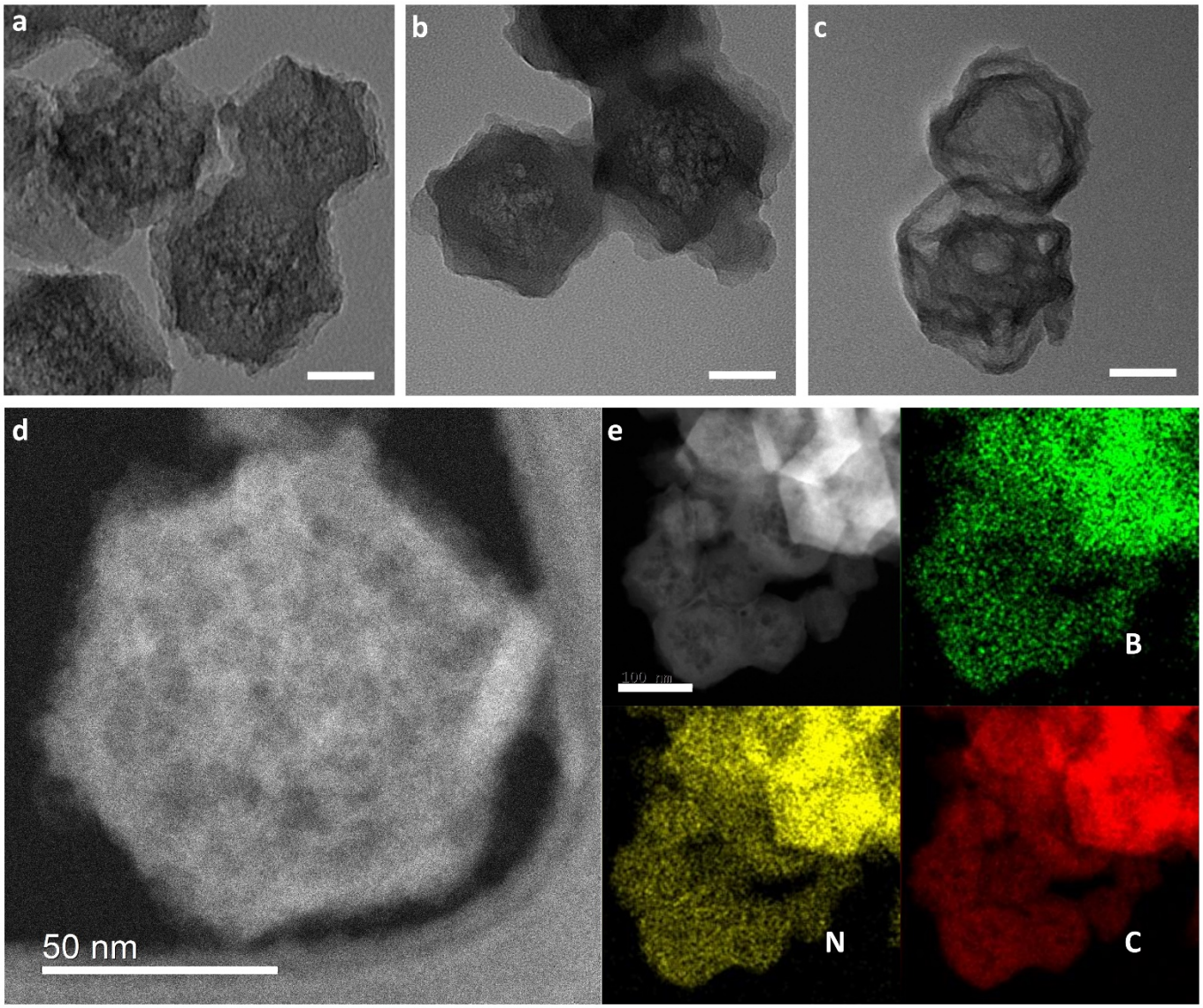

Fig. 3. Characterization of N@C and B,N@Cs. TEM images of (a) N@C, (b) B,N@C-AB, and (c) B,N@C-BA. All scale bars are 50 nm. (d) Aberration corrected HAADF-STEM, and (e) EDS mapping of B,N@C-AB, with the scale bar being 100 nm.

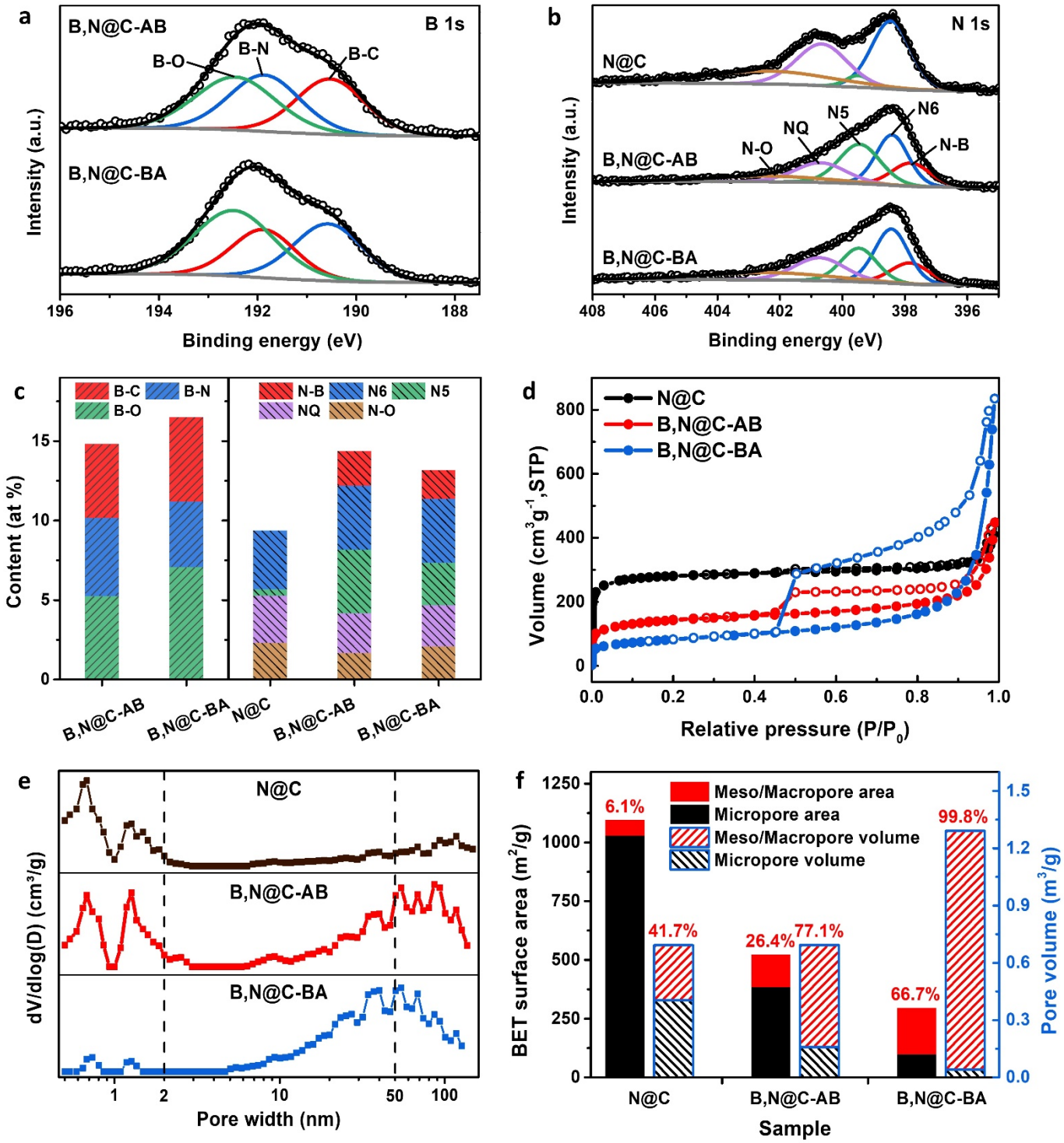

Fig. 4. Characterization of N@C and B,N@Cs. The high-resolution XPS spectra of (a) B 1 s, (b) N 1 s of N@C and B,N@C samples. (c) The contents of B and N determined by fitting the XPS spectra. (d) N_2 sorption isotherms at -196 °C, and (e) their corresponding pore size distributions (PSD) calculated using NL-DFT method, and (f) BET surface areas and pore volumes.

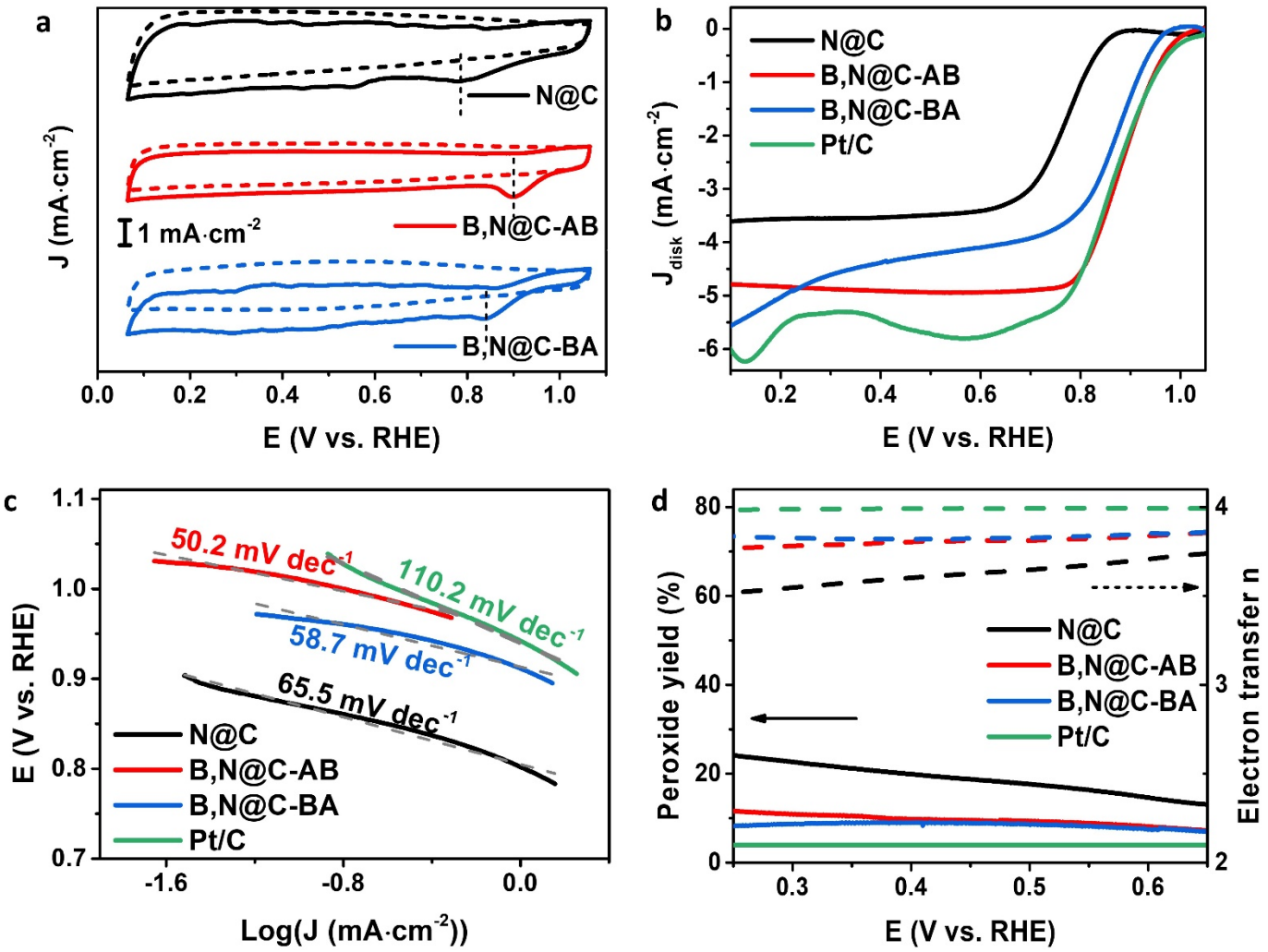

Fig. 5. Electrocatalytic performance for ORR in 0.1 M KOH electrolyte. (a) CV curves in N_2-saturated (dotted lines) and O_2-saturated (solid lines) alkaline electrolytes. (b) LSV curves with a fixed rotation rate of 1600 rpm at 10 mV s^{-1}. (c) Tafel plots and (d) Electron transfer number and H_2O_2 selectivity derived from LSV curves.